Electronic Supplementary Material (ESI) for Dalton Transactions.

High-Spin Carbonyl Complexes of Iron(I) and Cobalt(I)

Christian Schneider, Lukas Guggolz, C. Gunnar Werncke

Philipps-Universität Marburg, Fachbereich Chemie, Hans-Meerwein-Straße 4, D-35032 Marburg, Germany

Table of Contents

IR Spectra

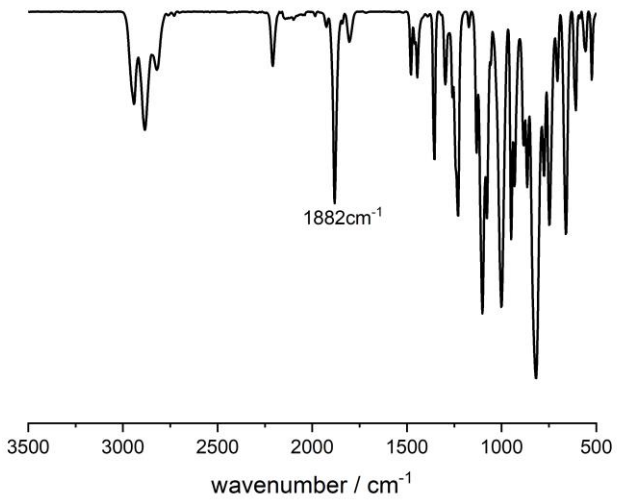

Figure S1. ATR IR spectrum of solid K{2.2.2crypt}[Co(CO)(hmds)$_2$], K{2.2.2crypt}[**1**].

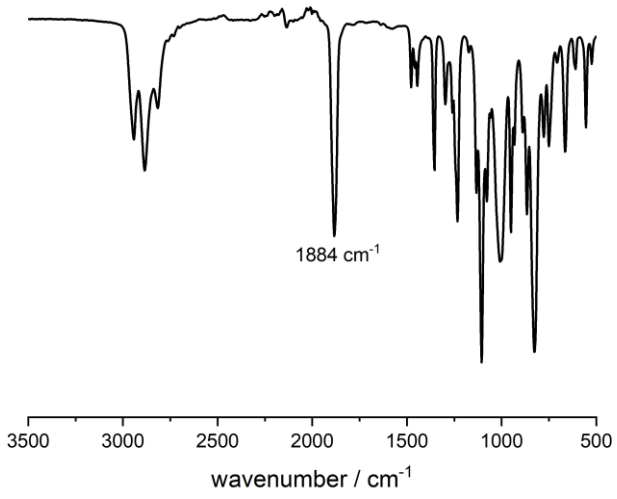

Figure S2. ATR IR spectrum of solid K{18c6}[Co(CO)(hmds)$_2$], K{18c6}[**1**].

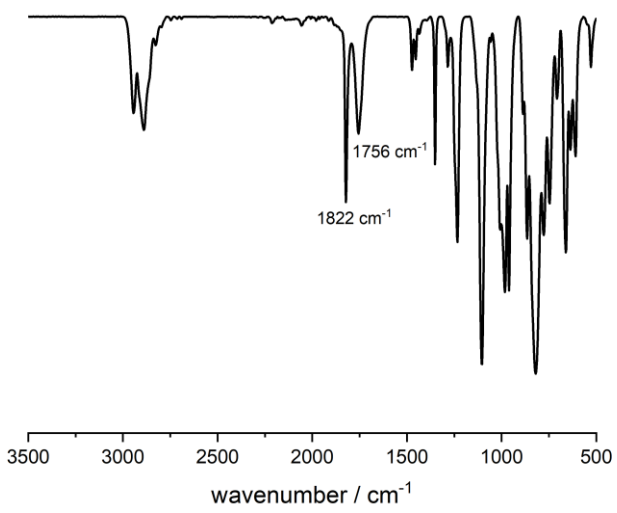

Figure S3. ATR IR spectrum of solid K{18c6}[Fe(CO)(hmds)$_2$], K{18c6}[**2**]. The band 1822 cm^{-1} is attributed to K{18c6}[**2**], whereas the signal at 1756 cm^{-1} belongs to an unkown secondary product (presumably [Fe(CO)$_4$]$^{2-}$).

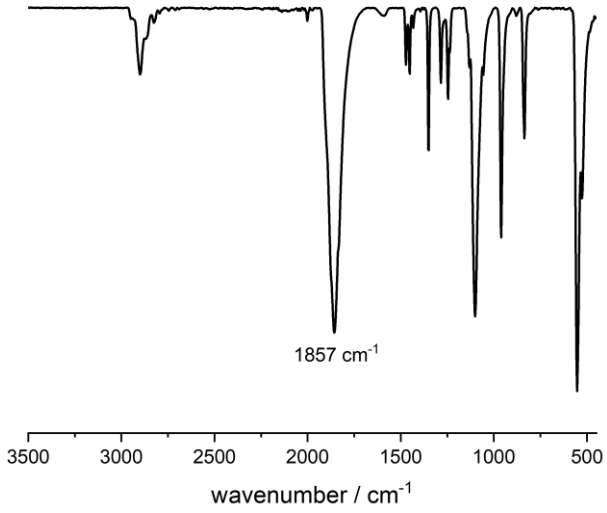

Figure S4. ATR IR spectrum of solid K{18c6}[Co(CO)$_4$], K{18c6}[**3**].

UV/VIS Spectra

The UV/VIS spectra were recorded on an *Analytik Jena Specord S600* spectrometer equipped with *UNISOKU CoolSpeK Cryostat*, using the WinASPECT software.

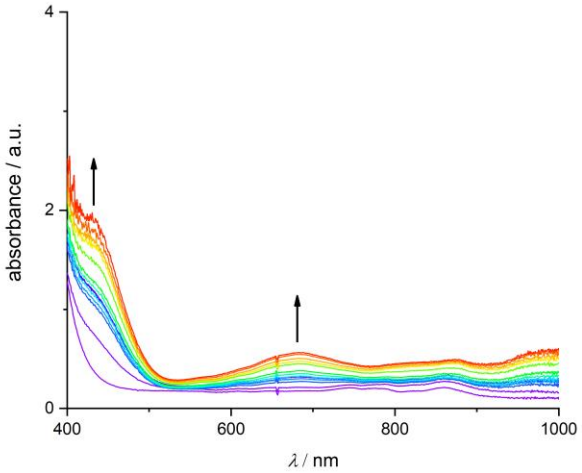

Figure S5. *In situ* UV/Vis spectra of the reaction of K{18c6}[Co(hmds)$_2$] with slight stoichiometric excess CO -80 °C in Et_2O. The arrows show bands at 430 nm and 638 nm which are attributed to K{18c6}[**1**]. To monitor the formation a spectrum was recorded every 40 seconds. The arrows show the direction of band evolution.

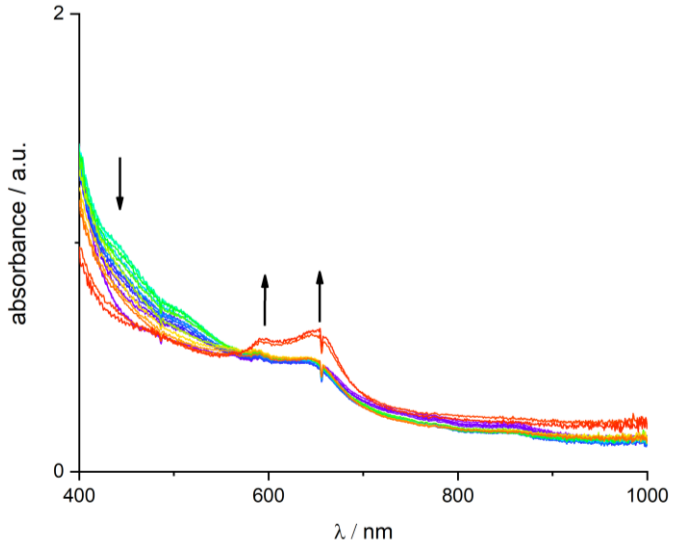

Figure S6. *In situ* UV/Vis spectra of the reaction of K{18c6}[Co(hmds)$_2$] with slight stoichiometric excess CO -80 °C in THF. The lack of a resolved band at 430 nm indicates the absence of K{m}[**1**]. The features at 590 and 660 nm resemble the ones observed for [**3**]$^-$ (see Figure S7). To monitor the reaction a spectrum was recorded every 30 seconds. The arrows show the direction of band evolution.

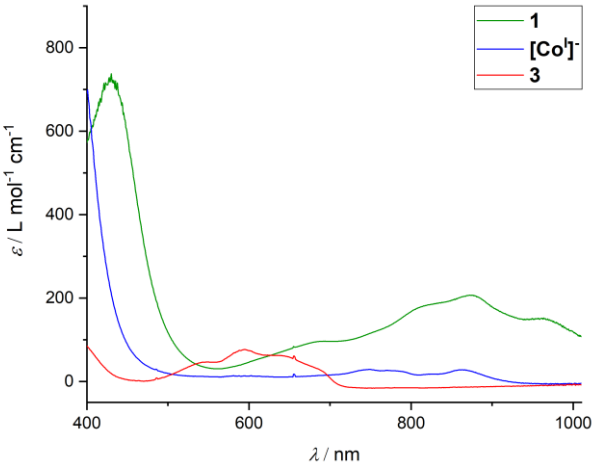

Figure S7. Overlay of the room temperature UV/VIS spectra of pristine K{m}[**1**] (green), K{18c6}[Co(hmds)$_2$] (blue) and K{18c6}[**3**] (red) dissolved in Et_2O. The spectrum of K{m}[**1**] shows decomposition as evidenced by pronounced bands above 700 nm in comparison with the signature attributed to in-situ formed K{m}[**1**] (see figure S5).

NMR spectra

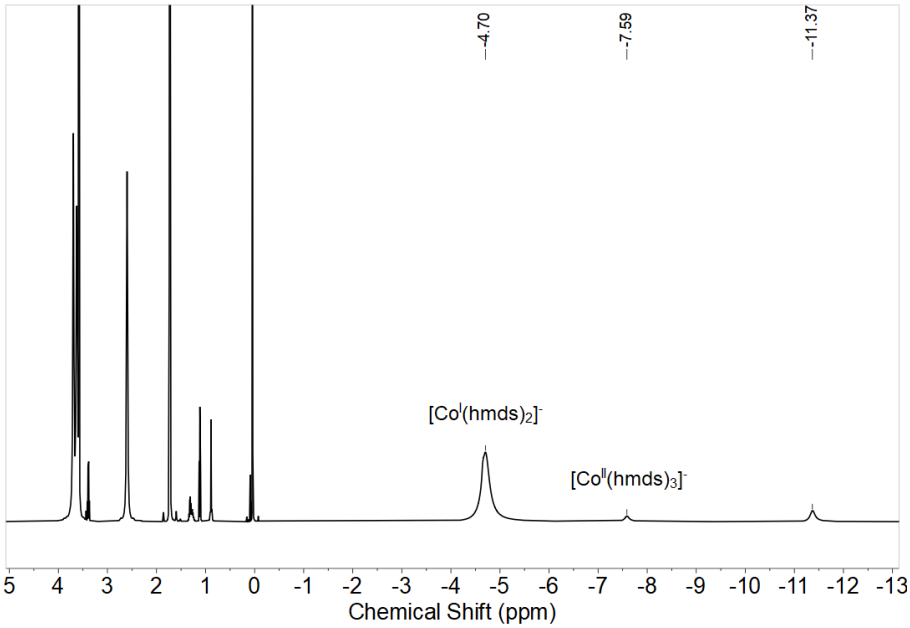

Figure S8. ^{1}H-NMR-spectrum of isolated K{2.2.2crypt}[**1**] dissolved in THF-d_8 showing only the [Co^I] starting complex, as well as minor amounts of [Co^{II}(hmds$_3$)]$^-$ decomposition product as well as an unknown species at -11.37 ppm.

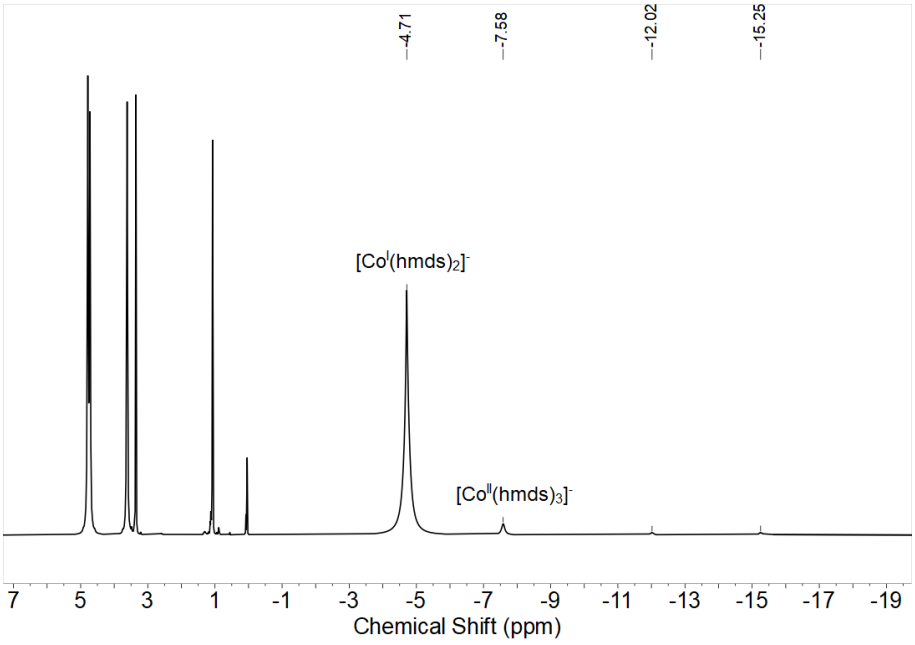

Figure S9. ^{1}H-NMR-spectrum of K{2.2.2crypt}[**1**] in Et_2O-d_{10} showing only the [Co^{I}] starting complex, the [Co^{II}(hmds$_3$)]$^-$ decomposition product as well as minor unknown species at −12.02 and −15.25 ppm.

Magnetic susceptibility measurements

Temperature-dependent magnetic DC susceptibility measurements were carried out with a *Quantum-Design Dynacool* PPMS system in the range from 295/300 to 3.0 K at a magnetic field of 0.1; 1.0 and 9.0 T. A powdered sample of K{18c6}[**1**] was capsuled in an polyurethane sample holder. The Magnetic moments of each raw data set were corrected according to the diamagnetic contribution of the sample holder and the sample using pascal constants[1], as well as the experimentally determined magnetic moment of the sample holder. Experimental c_MT vs. T data were modelled by Dr. S. Demeshko (University Göttingen) using a fitting procedure to the following spin Hamiltonian for one cobalt(I) S = 1 ion with Zeeman splitting and zero-field splitting:

$$\hat{H} = \mu_B \vec{B} \boldsymbol{g} \vec{S} + D\left[\hat{S}_z^2 - \frac{1}{3}S(S+1)\right]$$

Full-matrix diagonalization of the spin Hamiltonian was performed with the *julX_2s* program (E. Bill, Max-Planck Institute for Chemical Energy Conversion, Mülheim/Ruhr, Germany, **2014**). Matrix diagonalization is done with the routine ZHEEV from the LAPACK numerical package. Parameter optimization is performed with the simplex routine AMOEBA from NUMERICAL RECIPES. Temperature-independent paramagnetism (*TIP*) of 906·10^{-6} cm^{3}mol^{-1} was included according to $\chi_{calc} = \chi + TIP$.

Alternatively the paramagnetic susceptibilities were fitted with the Curie-Weiss-law $\chi_{CW} = (\frac{N_A \mu_B^2 n_{eff}}{3k_B})^2 \frac{1}{T-\theta}$, with $\chi_{para}T = (\chi_{TIP} + \chi_{CW})T$.

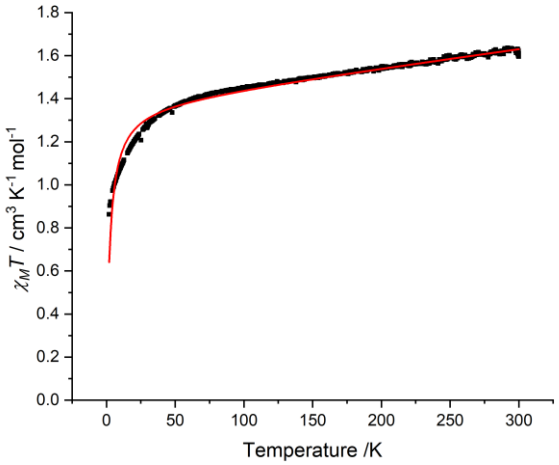

Figure S10. Plot of $\chi_M T$ vs. temperature for K{18c6}[**1**] with an applied field B = 0.1 T. μ_{eff} = 3.32 μ_B (300 K; $\mu_{S.O.}$ = 2.82 μ_B), θ = -2,36 K.

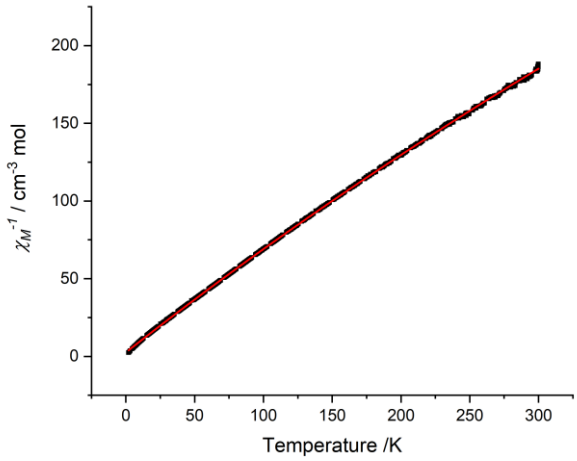

Figure S11. Temperature dependence of reciprocal molar magnetic susceptibility χ^{-1} of K{18c6}[**1**] with an applied field of B = 0.1 T.

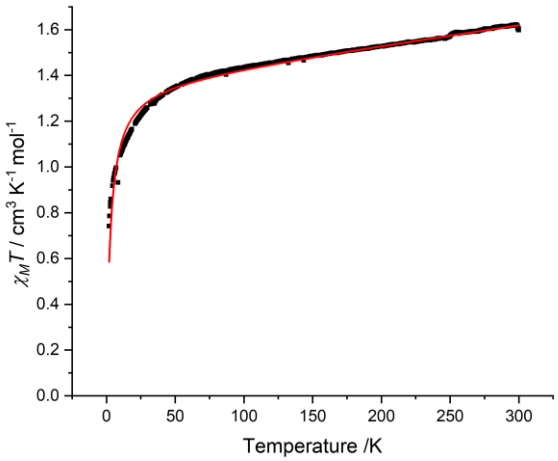

Figure S12. Plot of $\chi_M T$ vs. temperature for K{18c6}[**1**] with an applied field B = 1.0 T. μ_{eff} = 3.31 μ_B (300 K; $\mu_{S.O.}$ = 2.82 μ_B), θ = −2,75 K.

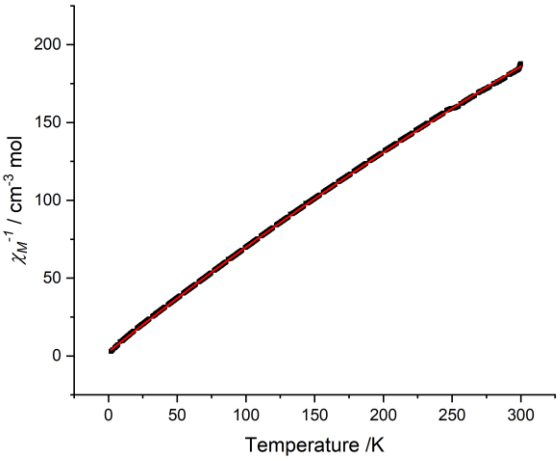

Figure S13. Temperature dependence of reciprocal molar magnetic susceptibility χ^{-1} of K{18c6}[**1**] with an applied field of B = 1.0 T.

Quantum chemical studies

All calculations were performed according to the specifications given in the experimental section in the manuscript. For compound [**2**]$^-$ we calculated both the high-spin and the low-spin state. The calculations were done without any symmetry restrictions.The differences between the calculated energy values given in Tables S5 and S6 can be attributed to the different approaches of the respective functionals: B97-D is a generalized gradient approximation (GGA) functional, while PBE0 and B3-LYP are hybrid functionals. Despite these differences, the calculated values add to the bigger picture and help to explain the experimental findings.

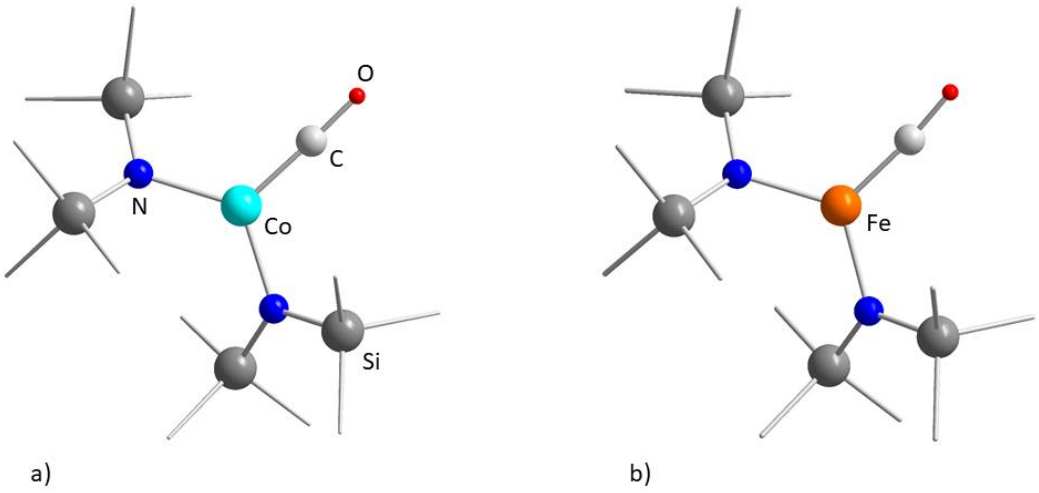

Figure S14. Computationally optimized molecular structures of a) complex [**1**]$^-$ and b) complex [**2**]$^-$ (high-spin). H atoms are omitted for clarity. The bond lengths and angles are given in Table 2 of the manuscript.

Table S1. Partial charges calculated by means of natural population analysis (NPA). The values for N and Si are averaged, due to the calculations being done without symmetry restrictions.

	[**1**]$^-$ (hs)	[**2**]$^-$ (hs)	[**2**]$^-$ (ls)
Co	+0.77	---	---
Fe	---	+0.95	+0.41
N	−1.72	−1.73	-1.59
C_{CO}	+0.28	+0.18	+0.44
O	−0.58	−0.61	-0.66
Si	+1.85	+1.84	-1.84

Table S2. Average atomic populations from spin density, calculated by means of NPA.

	[**1**]$^-$ (hs)	[**2**]$^-$ (hs)	[**2**]$^-$ (ls)
Co	1.93	---	---
Fe	---	3.10	1.26
C_{CO}	−0.14	−0.24	−0.22
O	−0.06	−0.10	−0.05
N	0.11	0.08	0.00
Si	0.00	0.00	0.00
C_{CH}	0.00	0.00	0.00
H	0.00	0.00	0.00

Table S3. Calculated shared electron numbers (SEN) of the respective M–C bonds and of a C–H bond as a comparison. Note that SEN are not absolute measures for the actual bond strength, but can be used to show trends.

	[**1**]$^-$ (hs)	[**2**]$^-$ (hs)	[**2**]$^-$ (ls)
Co–C	0.61	---	---
Fe–C	---	0.68	1.00
C–H	1.37	1.37	1.37

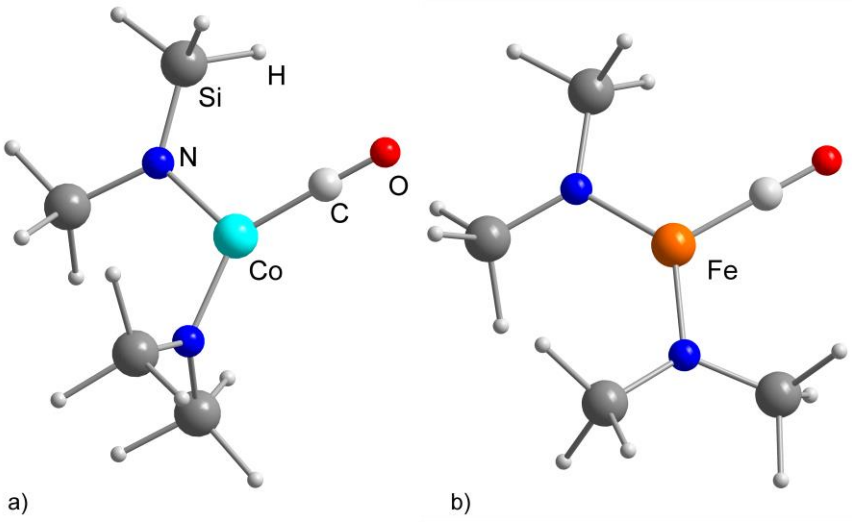

Figure S15. Computationally optimized molecular structures of **a)** complex $[Co(CO)\{N(SiH_3)_2\}_2]^-$ and **b)** $[Fe(CO)\{N(SiH_3)_2\}_2]^-$ (high-spin). The bond lengths and angles are given in Table S4.

Table S4. Calculated bond lengths (Å) and angles (°) of $[Co(CO)(N(SiH_3)_2)_2]^-$ and $[Fe(CO)(N(SiH_3)_2)_2]^-$.

	$[Co(CO)(N(SiH_3)_2)_2]^-$	$[Fe(CO)(N(SiH_3)_2)_2]^-$
M–N1	1.95	1.97
M–N2	1.94	1.97
M–C1	1.76	1.79
C1–O1	1.17	1.18
N1–M–C1	111	115
N2–M–C1	138	116
N1–M–N2	111	129

Table S5. Calculated energy differences ΔE (kcal/mol) between high-spin- and low-spin-[**2**]$^-$ obtained for three different functionals (with dispersion correction and Becke–Johnson damping).

Functional	h.s.-[**2**]$^-$	l.s.-[**2**]$^-$
B97-D	0.0	+6.5
PBE0	0.0	+17.9
B3-LYP	0.0	+13.4

Table S6. Calculated absolute energies (H_e) and reaction energies ΔE (kcal/mol) according to Scheme 1 in the manuscript obtained for three different functionals (with dispersion correction and Becke–Johnson damping).

Functional	$[Co(hmds)_2]^-$	CO	[**1**]$^-$	ΔE
B97-D	−3130.11956	−113.293223	−3243.46629	−33.5
PBE0	−3128.50987	−113.232308	−3241.78708	−28.2
B3-LYP	−3129.39578	−113.31208	−3242.74614	−24.0
Functional	h.s.-$[Fe(hmds)_2]^-$	CO	h.s.-[**2**]$^-$	ΔE
B97-D	−3010.9687	−113.293223	−3124.31378	−32.5
PBE0	−3009.45814	−113.232308	−3122.73382	−27.2
B3-LYP	−3010.33134	−113.31208	−3123.68227	−24.4
Functional	l.s.-$[Fe(hmds)_2]^-$	CO	l.s.-[**2**]$^-$	ΔE
B97-D	−3010.92141	−113.293223	−3124.30334	−55.6
PBE0	−3009.41437	−113.232308	−3122.70526	−36.7
B3-LYP	−3010.29065	−113.31208	−3123.66089	−36.5

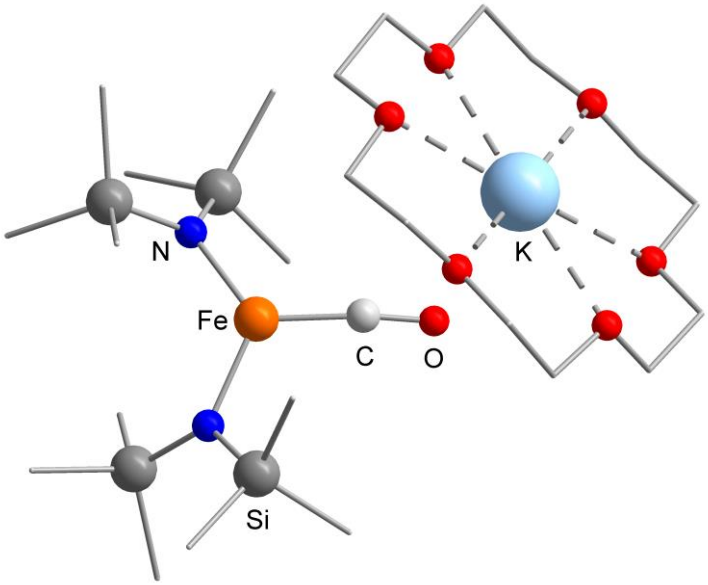

Figure S16. Computationally optimized molecular structure of K{18c6}**[2]**. The bond lengths and angles are given in Table S4. H atoms are omitted for clarity. Note that after the geometry optimization the cation is slightly tilted compared to the experimentally obtained structure. This is likely due to packing effects in the crystal, which cannot be reproduced by the computational methods used here.

Table S7. Calculated bond lengths (Å) and angles (°) of K{18c6}**[2]**.

	K{18c6}**[2]**
M–N1	1.98
M–N2	1.98
M–C1	1.78
C1–O1	1.19
O–K	2.88
N1–M–C1	116
N2–M–C1	118
N1–M–N2	121

X-Ray diffraction analysis and molecular structures

Table S8. Crystal data and structure refinement for K{2.2.2crypt}[**1**].

Empirical formula	$C_{31}H_{72}CoKN_4O_7Si_4$
Formula weight	823.31
Temperature/K	100.0
Crystal system	triclinic
Space group	P-1
a/Å	12.5496(5)
b/Å	13.9247(6)
c/Å	15.1024(6)
α/°	111.7110(10)
β/°	92.9320(10)
γ/°	108.9010(10)
Volume/Å^3	2275.40(16)
Z	2
ρ_{calc}g/cm^3	1.202
μ/mm^{-1}	0.616
F(000)	888.0
Crystal size/mm^3	0.416 × 0.13 × 0.117
Radiation	MoKα (λ = 0.71073)
2Θ range for data collection/°	4.42 to 52.164
Index ranges	-15 ≤ h ≤ 14, -17 ≤ k ≤ 17, -18 ≤ l ≤ 18
Reflections collected	41838
Independent reflections	9004 [R_{int} = 0.0557, R_{sigma} = 0.0422]
Data/restraints/parameters	9004/0/445
Goodness-of-fit on F^2	1.026
Final R indexes [I>=2σ (I)]	R_1 = 0.0382, wR_2 = 0.0810
Final R indexes [all data]	R_1 = 0.0593, wR_2 = 0.0881
Largest diff. peak/hole / e Å^{-3}	0.32/-0.43

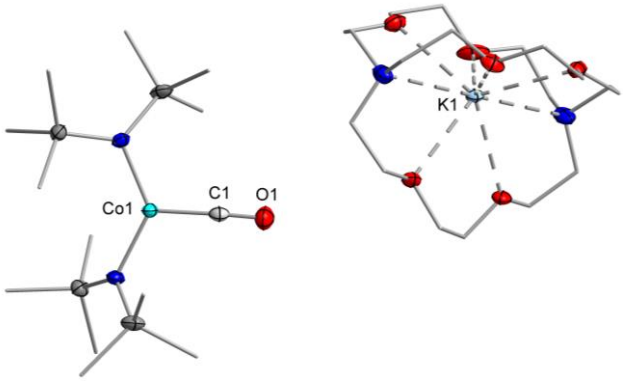

Figure S17. Molecular structure of K{2.2.2crypt}[**1**] within the crystal. Hydrogen atoms have been omitted for clarity.

Table S9. Crystal data and structure refinement for K{18c6}[**2**]**.**

Empirical formula	$C_{25}H_{60}FeKN_2O_7Si_4$
Formula weight	708.06
Temperature/K	100.01
Crystal system	monoclinic
Space group	$P2_1/c$
a/Å	8.6181(5)
b/Å	19.9580(10)
c/Å	23.1156(12)
α/°	90
β/°	90.923(2)
γ/°	90
Volume/Å^3	3975.4(4)
Z	4
ρ_{calc}g/cm^3	1.183
μ/mm^{-1}	0.641
F(000)	1524.0
Crystal size/mm^3	0.475 × 0.211 × 0.114
Radiation	MoKα (λ = 0.71073)
2Θ range for data collection/°	4.446 to 52.142
Index ranges	-10 ≤ h ≤ 9, -24 ≤ k ≤ 24, -28 ≤ l ≤ 28
Reflections collected	29271
Independent reflections	7815 [R_{int} = 0.0564, R_{sigma} = 0.0524]
Data/restraints/parameters	7815/0/373
Goodness-of-fit on F^2	1.023
Final R indexes [I>=2σ (I)]	R_1 = 0.0328, wR_2 = 0.0638
Final R indexes [all data]	R_1 = 0.0528, wR_2 = 0.0695
Largest diff. peak/hole / e Å^{-3}	0.30/-0.28

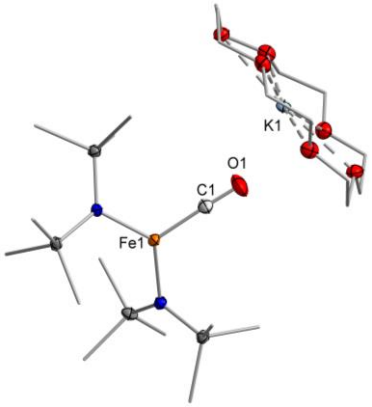

Figure S18. Molecular structure of K{18c6}[**2**] within the crystal. Hydrogen atoms have been omitted for clarity.

Table S10. Crystal data and structure refinement for K{18c6}[**3**].

Empirical formula	$C_{16}H_{24}CoKO_{10}$
Formula weight	474.43
Temperature/K	100.0
Crystal system	trigonal
Space group	R3
a/Å	13.8148(9)
b/Å	13.8148(9)
c/Å	9.9198(7)
α/°	90
β/°	90
γ/°	120
Volume/Å^3	1639.5(2)
Z	2.9997
ρ_{calc}g/cm^3	1.441
μ/mm^{-1}	1.022
F(000)	738.0
Crystal size/mm^3	0.306 × 0.216 × 0.118
Radiation	MoKα (λ = 0.71073)
2Θ range for data collection/°	5.334 to 54.218
Index ranges	−17 ≤ h ≤ 17, −17 ≤ k ≤ 17, −12 ≤ l ≤ 12
Reflections collected	10135
Independent reflections	1617 [R_{int} = 0.0677, R_{sigma} = 0.0475]
Data/restraints/parameters	1617/1/86
Goodness-of-fit on F^2	1.067
Final R indexes [I>=2σ (I)]	R_1 = 0.0357, wR_2 = 0.0779
Final R indexes [all data]	R_1 = 0.0404, wR_2 = 0.0798
Largest diff. peak/hole / e Å^{-3}	0.47/-0.20
Flack parameter	0.40(3)*

* The structure was refined as a twin, twin ratio refined to 0.40(3).

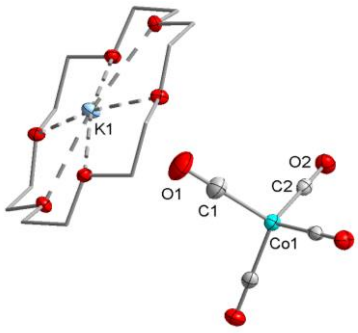

Figure S19. Molecular structure of K{18c6}[**3**] within the crystal. Hydrogen atoms have been omitted for clarity.

References

[1] G. A. Bain, J. F. Berry, *J. Chem. Educ.* **2008**, *85*, 532–536.